Shubnikov–de Haas Quantum Oscillations with Large Spin Splitting in High-Mobility $Al_{0.8}Ga_{0.2}Sb/InAs/Al_{0.8}Ga_{0.2}Sb$ Quantum-Well Heterostructures

Zhenghang Zhi(职正航)[1†], Hanzhi Ruan(阮涵之)[1†], Jiuming Liu(刘久铭)[1], Xinpeng Li(李信朋)[1], Yong Zhang(张勇)[1], Qi Yao(姚岐)[2,3], Chenjia Tang(汤辰佳)[2,3], Yujie Xiao(肖裕杰)[3], and Xufeng Kou(寇煦丰)[1,2*]

[1]*School of Information Science and Technology, ShanghaiTech University, Shanghai 201210, China*
[2]*ShanghaiTech Laboratory for Topological Physics, ShanghaiTech University, Shanghai 200031, China*
[3]*School of Physical Science and Technology, ShanghaiTech University, Shanghai 201210, China*

(Received 28 April 2025; accepted manuscript online 26 August 2025)

We report the epitaxial growth of high-quality $Al_{0.8}Ga_{0.2}Sb/InAs/Al_{0.8}Ga_{0.2}Sb$ quantum well films characterized by high carrier mobility and strong spin–orbit coupling. By appropriately optimizing the Al-to-Ga ratio in the AlGaSb barrier layer, the quantum confinement of the heterostructure is significantly enhanced. Alongside a giant magnetoresistance ratio of 3.65×10^5%, the two-carrier transport model from Hall measurements reveals an ultra-high electron mobility of $7.18 \times 10^5\,\mathrm{cm^2 \cdot V^{-1} \cdot s^{-1}}$ at low temperatures. Meanwhile, pronounced Shubnikov–de Haas (SdH) quantum oscillations persist up to 30 K, and their single-frequency feature indicates a well-defined Fermi surface without subband mixing in the two-dimensional electron gas channel. Moreover, the large effective g-factor and tilted-field-induced orbital effect lead to the observation of split SdH peaks at large magnetic fields. Our results validate that AlGaSb/InAs quantum well heterostructures are suitable candidates for constructing energy-efficient topological spintronic devices.

DOI: 10.1088/0256-307X/42/9/090708 CSTR: 32039.14.0256-307X.42.9.090708

Benefiting from high electron mobility, strong spin–orbit coupling, small effective electron mass, and narrow direct bandgap, InAs and InSb are highly promising for high-speed electronic, spintronic, and infrared optoelectronic applications.[1–3] In particular, InAs/GaSb-based heterostructures have emerged as an intriguing platform, as their type-Ⅱ band alignment gives rise to non-trivial topological edge states under an appropriate band-inversion configuration.[4] For instance, recent advancements in the fabrication of nanoscale InAs/GaSb quantum wells (QWs) have demonstrated the realization of the quantum spin Hall effect,[5] manifesting robust edge states protected by time-reversal symmetry (TRS).[3,6] On the other hand, breaking TRS can lead to an unconventional excitonic topological order in the heterostructure system under imbalanced electron and hole densities.[7] In addition to such unique topological features, the InAs/GaSb hetero-interfaces not only host a well-defined two-dimensional electron gas (2DEG) channel with ultra-high carrier mobility but also warrant effective manipulation of spin states through the interfacial Rashba effect.[8]

Despite the aforementioned attributes, the practical implementation of InAs/GaSb heterostructures faces several challenges, primarily due to the narrow bandgap nature of GaSb, which cannot provide an insulating barrier layer and invariably brings about leakage currents and reduced thermal stability.[9] Alternatively, previous studies have explored several ternary or quaternary compound semiconductors (e.g., InGaAs, InAlAs, InGaAsSb, and InPAsSb) as a more viable buffer layer option for constructing high-performance InAs electronic device applications.[10] In this context, it is validated that the enlarged bandgap of AlGaSb ensures superior quantum confinement of carriers within the InAs/AlGaSb interface, resulting in high mobility[11] and increased spin injection and detection efficiencies.[12] Moreover, by adjusting the Al and Ga composition, the lattice constant of AlGaSb can be finely tuned to achieve better lattice matching with InAs, thereby reducing interface defects.[13]

In this work, we report the growth and characterization of high-quality $Al_{0.8}Ga_{0.2}Sb/InAs/Al_{0.8}Ga_{0.2}Sb$ QWs using molecular beam epitaxy (MBE). Guided by the band diagram from TCAD simulations, the optimized sample structure exhibits an ultra-high electron mobility of $7.18 \times 10^5\,\mathrm{cm^2 \cdot V^{-1} \cdot s^{-1}}$ and a Fermi velocity of 7.16×10^5 m/s, enabling observations of a giant magnetoresistance ratio above 10^5% and pronounced Shubnikov–de-Haas (SdH) quantum oscillations up to $T = 30$ K. Additionally, the angular dependence of the SdH oscillations reveals a large spin splitting with a g-factor of 12.93. Our findings demonstrate that optimizing the Al/Ga ratio in the AlGaSb barrier layer can effectively enhance the magneto-transport properties of the InAs/AlGaSb QW

†These authors contributed equally to this work.
*Corresponding author. Email: kouxf@shanghaitech.edu.cn
© 2025 Chinese Physical Society and IOP Publishing Ltd. All rights, including for text and data mining, AI training, and similar technologies, are reserved.

system, and they also provide a foundation for the development of next-generation high-speed electronic and spintronic devices.

The goal of this work is to enhance the electrical performance of InAs/AlGaSb through QW structural engineering, which includes dedicated designs for the thickness and component ratio of the AlGaSb barrier layer. Accordingly, we first applied TCAD simulation (i.e., which takes into account polarization models, field-dependent mobility models, and Shockley–Read–Hall models) to investigate the band diagram of the InAs/AlGaSb QW heterostructures.[14] As illustrated in Fig. 1(a), the optimized structure consists of an $Al_{0.8}Ga_{0.2}Sb$ (10 nm)/InAs (20 nm)/$Al_{0.8}Ga_{0.2}Sb$ (20 nm) tri-layer configuration, with an Al-to-Ga ratio of 4 to ensure a well-defined QW while compromising on lattice mismatch between InAs and AlGaSb. Based on the simulation results, high-quality $Al_{0.8}Ga_{0.2}Sb$/InAs/$Al_{0.8}Ga_{0.2}Sb$ thin films were grown on n-type conductive GaSb(100) substrate by MBE. In particular, the GaSb substrate was pre-annealed at 530 ℃ under a Sb-rich environment to remove the native oxide layer; this pre-anneal process was completed by observing (2 × 6) surface reconstruction using an *in situ* reflective high-energy electron diffractometer (RHEED) pattern. Afterwards, a 1 µm-thick insulating AlGaAsSb (i.e., E_g = 1.5 eV) was introduced as a buffer layer to electrically isolate the QW from the conductive substrate (i.e., with substrate temperature kept at 400 ℃).[15] After buffer layer growth, the $Al_{0.8}Ga_{0.2}Sb$ (10 nm)/InAs (20 nm)/$Al_{0.8}Ga_{0.2}Sb$ (20 nm) QW structure was deposited according to TCAD simulation results; thus, the Al-to-Ga ratio was precisely adjusted using a beam flux monitor. Finally, a heavily-doped InAs capping layer (2 nm) was grown to protect the AlGaSb barrier from oxidation as well as facilitate Ohmic contact formation for device fabrication.

It is worth noting that a 2D streaky RHEED pattern persisted during entire growth phases, validating epitaxial growth mode without involving lattice mismatch-induced macro-structural defects. Concurrently, the cross-sectional transmission electron microscopy (TEM) image also manifests absence of macroscopic threading dislocations in well-established QW structure with sharp interfaces (i.e., detailed material characterizations of our MBE-grown InAs/GaSb-based heterostructures are reported in our previous work[16,17]). After sample growth, we fabricated InAs/AlGaSb QW film into µm-sized six-terminal Hall bar devices by standard nano-fabrication process. As displayed in inset Fig. 1(b), etching process precisely controlled stop at insulating AlGaAsSb buffer layer avert shorting with conductive GaSb substrate. Meanwhile, low-resistance Ohmic contacts defined depositing Ti (20 nm)/Au (100 nm) using electron-beam evaporator (e-beam) and rapid thermal annealing methods.

Subsequently, temperature-dependent magneto-transport measurements were conducted on the InAs/AlGaSb QW-based devices where an AC current ($|I|$ = 1 µA, f = 67 Hz) was applied along the x-axis, while longitudinal (V_{xx}) and transverse (V_{xy}) voltages were simultaneously recorded using the SR830 lock-in amplifier. The temperature-dependent resistance curve exhibits a typical metallic R–T behavior, namely that the channel resistance decreases successively as the base temperature drops from T = 298 K to 50 K [Fig. 1(b)], indicating the presence of a 2DEG channel in the InAs/AlGaSb QW heterostructure at low temperatures.[18,19] Concurrently, the non-linear Hall curves observed in the low-field region [Fig. 1(c)] suggest multi-channel conduction characteristics.[20] By applying the two-carrier transport model, room-temperature carrier mobility and concentration of both n-type and p-type channels are extracted to be $\mu_n = 5.42\times10^3\,\mathrm{cm^2\cdot V^{-1}\cdot s^{-1}}$, $n_{2D} = -5.57\times10^{12}\,\mathrm{cm^{-2}}$, and $\mu_p = 479\,\mathrm{cm^2\cdot V^{-1}\cdot s^{-1}}$, $p_{2D} = +8.2\times10^{12}\,\mathrm{cm^{-2}}$.[21] Following the same data fitting process, figure 1(d) summarizes the evolutions of electron mobility (red triangles) and density (blue stars) with respect to temperature. It is seen that electron density continuously decreases from 298 K to 50 K, mainly due to thermally suppressed impurity ionization rate in bulk InAs layer.[22,23] As the Hall-bar device further cools down below 50 K, bulk conduction is almost frozen out,[24] leaving confinement of itinerant electrons within the 2DEG channel at both InAs/AlGaSb hetero-interfaces with an electron density of $n_{2D} = 2.31\times10^{12}\,\mathrm{cm^{-2}}$ at T = 1.5 K (i.e., it is mentioned that Hall-derived carrier density is higher than SdH-derived carrier density which only reflects high-mobility carriers[25]). As a result, such 2DEG-dominated transport characteristics endow dramatic enhancement of carrier mobility in low-temperature regions.

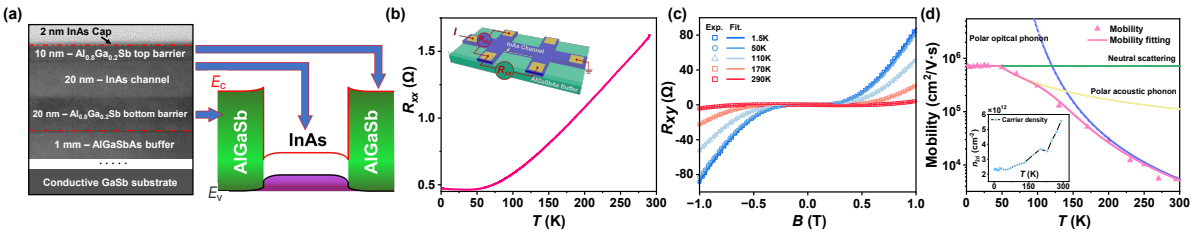

Fig. 1. (a) Left: Cross-sectional TEM image shows the well-ordered crystalline configuration. All the interfaces are distinguished without notable defects. Right: The band diagram of the $Al_{0.8}Ga_{0.2}Sb$/InAs/$Al_{0.8}Ga_{0.2}Sb$ QW by TCAD simulation. (b) Temperature-dependent resistance of the MBE-gorwn AlGaSb/InAs/AlGaSb sample. Inset: Illustration of the six-terminal hall bar device. (c) Non-linear Hall curves in the low-field region and two-carrier model fitting results (solid lines). (d) Temperature-dependent mobility (triangle symbols) of the AlGaSb/InAs-based QW sample. The μ–T slope can be well-fitted by Eq. (1) where various scattering mechanisms dominate at different temperature regions. Inset: Corresponding temperature evolution of the electron density n_{2D} extracted from the Hall measurements.

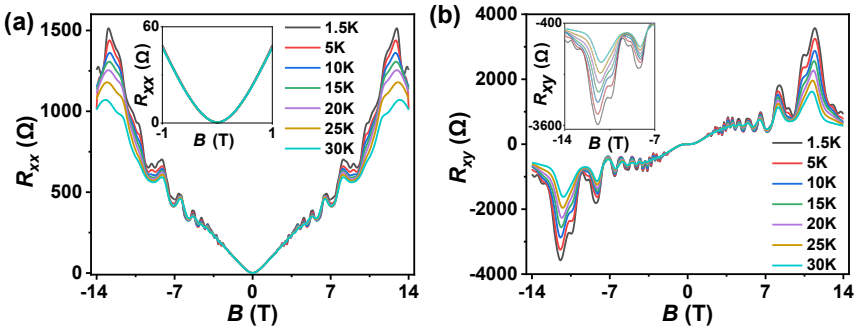

Fig. 2. (a) Temperature-dependent magnetoresistance results of the InAs/AlGaSb QW sample with pronounced SdH oscillations from 1.5 K to 30 K. Inset: Parabolic MR curve observed in the low magnetic-field region. (b) Temperature-dependent Hall resistance of InAs/AlGaSb QW sample. The peaks and valleys of R_{xy} are consistent with the R_{xx} data. Inset: Observation of the double-split SdH peaks in the high magnetic-field region.

As long as phonon scatterings (e.g., polar acoustic/optical phonon scatterings) are suppressed, electron mobility increases from $5.42 \times 10^3\,\mathrm{cm^2{\cdot}V^{-1}{\cdot}s^{-1}}$ (298 K) to $6.77 \times 10^5\,\mathrm{cm^2{\cdot}V^{-1}{\cdot}s^{-1}}$ (50 K), corresponding to a 125 times enhancement. Notably, the mobility of our sample reached a peak value of $\mu = 7.18 \times 10^5\,\mathrm{cm^2{\cdot}V^{-1}{\cdot}s^{-1}}$ at $T = 1.5$ K, and saturation behavior at $T < 25$ K reflects that neutral impurity scattering dominates in deep cryogenic temperature region (i.e., it is noted that carrier mobility obtained by Hall measurement is higher than quantum mobility extracted from SdH quantum oscillation due to longer transport lifetime[26]). Quantitatively, overall μ_{n}–T curve can be described by applying Matthiessen's rule,[27]

$$\mu_{\mathrm{n}} = (1/\mu_{\mathrm{POP}} + 1/\mu_{\mathrm{PE}} + 1/\mu_{\mathrm{NE}})^{-1}, \tag{1}$$

where μ_{POP}, μ_{PE}, and μ_{NE} correspond to the contributions from the thermally-activated polar optical phonon scattering, polar acoustic phonon scattering, and neutral impurity scattering, respectively. Among them, polar optical phonon scattering and polar acoustic phonon scattering (i.e., $\mu_{\mathrm{POP}} \propto T^{-4.03}$ and $\mu_{\mathrm{PE}} \propto T^{-1.5}$) are temperature-dependent,[28,29] whereas μ_{NE} is regarded as a temperature-independent term since it mainly rises from the static impurity scattering in the 2DEG channels. Based on the fitting result shown in Fig. 1(c), it is seen that these three scattering mechanisms dominate in different temperature regimes, and the fitted data (solid line) are closely aligned with the experimental data (triangle symbol), unveiling the physical origin of the high-mobility InAs/AlGaSb QW system.

To further investigate the electrical properties of our MBE-grown samples, high magnetic-field measurements were conducted at various temperatures. As shown in Fig. 2(a), the longitudinal resistance R_{xx} exhibits a typical parabolic behavior in the low-magnetic field region, and a giant magnetoresistance ratio of $\mathrm{MR} = \frac{\rho_{xx}(B)-\rho_{xx}(0)}{\rho_{xx}(0)} \times 100\% = 3.64 \times 10^5\%$ is obtained at $B = 14$ T. Strikingly, thanks to the high-mobility nature of the InAs/AlGaSb QW samples, pronounced SdH quantum oscillations are observed from $T = 1.5$ K to $T = 30$ K (Fig. 2). Given the correlation of $\tau = \mu/m^*$, such a high carrier mobility also warrants a long scattering time (τ) in the 2DEG channels, which ensures that electrons can coherently complete several cyclotron orbits before being scattered (i.e., $\omega_{\mathrm{c}}\tau \gg 1$, where ω_{c} is the resonance frequency).[30] Likewise, according to $\omega_{\mathrm{c}} = eB/m^*$, the small effective mass of InAs is able to satisfy the $\hbar\omega_{\mathrm{c}} \gg k_{\mathrm{B}}T$ condition in the low-temperature region, which in turn contributes to a marked Landau level (LL) energy gap splitting.[31] As a result, the initiation of the SdH oscillation of our device is found to occur at a relatively low-magnetic field of $B = 2.5$ T at 1.5 K. In alignment with Fig. 2(a), the Hall resistance R_{xy} also displays well-resolved quantum oscillations, with its peak and valley positions consistent with the R_{xx} data [i.e., yet due to the high carrier density, quantum Hall effects are not observed in the present device without gate tuning]. Besides, it is noted that a unique double-peak feature is observed in the high magnetic-field region [inset of Fig. 2(b)], which will be addressed in the following section.

Based on these SdH oscillation results, quantitative analyses were further carried out to extract associated electrical parameters. Figure 3(a) displays the temperature-dependent SdH oscillation signals after removing their parabolic MR backgrounds. It is seen that the oscillation peak and valley positions remain almost unchanged with temperature, indicating a stable carrier density and a well-defined Fermi surface.[32] This temperature-invariant periodicity also suggests the well-developed LLs unaffected by thermal broadening.[33] In the meantime, the amplitudes of the SdH oscillation curves stay around 300 Ω in the entire [1.5 K, 30 K] region, again epitomizing the high carrier mobility, long quantum coherence time, and negligible impurity/interface scattering characteristics of our MBE-grown InAs/AlGaSb QW sample. Moreover, taking advantage of both the robust quantum confinement and the salient interface quality, the supplementary fast Fourier transform (FFT) data in Fig. 3(b) reveal a single oscillating frequency of $f_{\mathrm{SdH}} = 31.1$ T, which indicates that quantum oscillation mainly originates from the high-mobility 2DEG channel without invoking additional parallel conduction channels (i.e., the hole mobility of the p-type channel is too low to trigger another SdH oscillation pattern) nor sub-band mixing at deep cryogenic temperatures.[34] According to the Onsager formula of $F = (\Phi_0/2\pi^2)S_{\mathrm{F}}$ (where $\Phi_0 = \frac{h}{2e}$),[35] the Fermi surface can be obtained

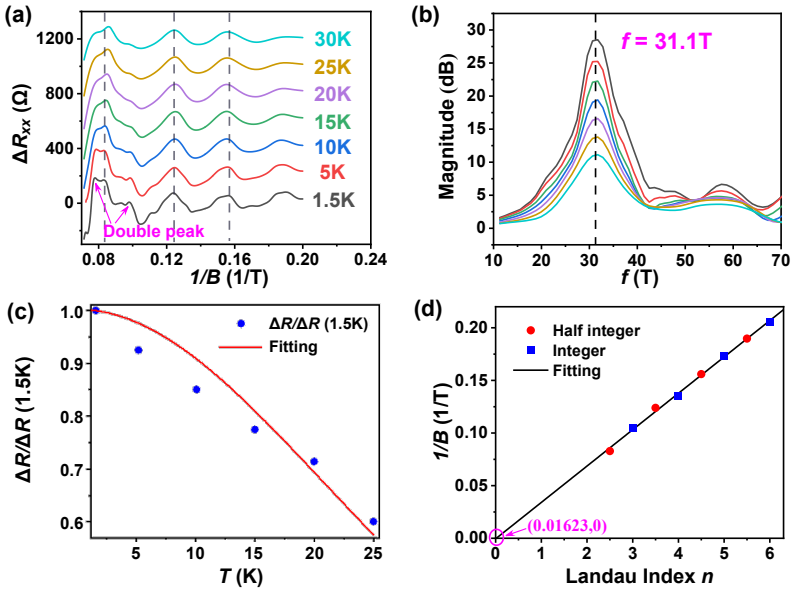

Fig. 3. (a) Temperature-dependent SdH oscillation signals after removing the parabolic backgrounds. (b) FFT of the SdH oscillations with a single frequency of $f = 31.1$ T. (c) Temperature-dependent normalized SdH oscillation amplitude (blue circles) and the fitting results (red dashed line) using the LK theory. (d) LL index plot where integers and half integers are represented by blue circles and red squares, respectively.

as $S_{\rm F} = 2.969 \times 10^{-3}\,\text{Å}^{-2}$, and the corresponding Fermi momentum is $k_{\rm F} = \sqrt{S_{\rm F}/\pi} = 0.0307\,\text{Å}^{-1}$. Subsequently, figure 3(c) illustrates a negative correlation between the normalized SdH oscillation amplitude $\Delta R(T)/\Delta R(1.5\,\text{K})$ and temperature. It is recalled that electrons would be thermally excited across adjacent LLs, and the occupation of these levels invariably becomes less distinct due to thermal smearing, thereby diminishing the amplitude of the SdH oscillation. Quantitatively, the extent of this thermal damping is explained by the Lifshitz–Kosevich (LK) theory, where the amplitude of $\Delta R_{xx}(T)$ is given by[36]

$$\Delta R_{xx}(T) \propto \frac{\lambda(T)}{\sinh\lambda(T)} \mathrm{e}^{-\lambda(T)}, \tag{2}$$

where $\lambda(T) = \frac{2\pi^2 k_{\rm B} T m_{\rm cyc}}{\hbar e B}$ is the thermal factor. By fitting the measured curve of Fig. 3(c), the effective mass of electrons and the Fermi velocity are extracted to be $m_{\rm cyc} = 0.0497 m_{\rm e}$ and $v_{\rm F} = \frac{\hbar k_{\rm F}}{m_{\rm cyc}} = 7.155 \times 10^5\,\text{m}\cdot\text{s}^{-1}$.

To understand the origin of the SdH oscillations and gain insight into the band dispersion near the Dirac point, we constructed the LL fan diagram by plotting $1/B$ as a function of the Landau index. It is observed from Fig. 3(d) that the $\Delta R_{xx}(T)$ peak-and-valley positions (i.e., the half-integer and integer LL indices) are linear with $1/B$, and the Landau index n-axis intercept n_x is nearly zero. Combined with the expression of $\phi_{\rm B} = \pi(1 - 2\gamma)$ where $\gamma = \frac{1}{2} - n_x = \frac{1}{2}$,[37,38] it is found that the Berry phase $\phi_{\rm B}$ of the 2DEG channel is zero in our AlGaSb/InAs/AlGaSb sample (i.e., which is different from GaSb/InAs QW counterpart with a topologically non-trivial edge state and a non-zero Berry phase of π[39]). In this regard, it is proposed that on one hand, introducing Al enlarges the bandgap of the AlGaSb barrier layer, enhancing quantum confinement to boost mobility. On the other hand, as Al content increases, type-Ⅱ QW-induced band inversion may no longer hold; thus, band alignment of InAs/AlGaSb gradually transits from type-Ⅱ to type-I, as confirmed by TCAD simulation data [Fig. 1(a)]. Therefore, our results justify the importance of barrier layer composition in determining magneto-transport behaviors of InAs-based QW systems.

In addition to SdH oscillations, it is known that the spin imbalance and electron–electron interactions in the presence of large perpendicular magnetic fields can lead to an enhancement of the effective g-factor.[40] To address this point, angular-dependent magneto-transport measurements were conducted, and the resulting SdH oscillation curves are summarized in Fig. 4(b). It is discovered that when the tilt angle θ between the magnetic field and the z-axis (i.e., normal to the sample plane) increases from 45° to 60°, the SdH oscillation curve experiences a 180° phase shift; namely, its peaks and valleys are reversed in the same ΔR_{xx}–$B\cos(\theta)$ diagram, as indicated by the red and blue arrows. Under such circumstances, by applying the coincidence method $g^* = \frac{m_{\rm e}}{m_{\rm cyc}}\cos\Theta_0$ (where g^* is the effective g-factor, and Θ_0 is the critical coincidence angle in reference to inversion of SdH oscillation amplitude[41]), we find that the effective g-factor of our MBE-grown InAs/AlGaSb QW sample is $g^* = 12.93$ (i.e., it is noted that this value closely correlates with quantum-well band structures; therefore its value may vary among different InAs-based heterostructure systems[36–39]). Along with strong intrinsic spin–orbit coupling of InAs, such a large g-factor leads to an evident spin-splitting of SdH oscillations in high-field regions. As highlighted by arrows in Figs. 3(a) and 4(c), temperature-dependent double peaks appear for SdH oscillations at $B = 10.5$ T and 12.2 T for $T < 10$ K (i.e., which differs from onset temperature of SdH oscillation). Given relation between LL energy and Zeeman splitting energy: $E_n = \hbar\omega_{\rm c}(n+\frac{1}{2}) + \frac{1}{2}g^*\mu_{\rm B}B$, these double-split peaks may originate from Zeeman effect.[42]

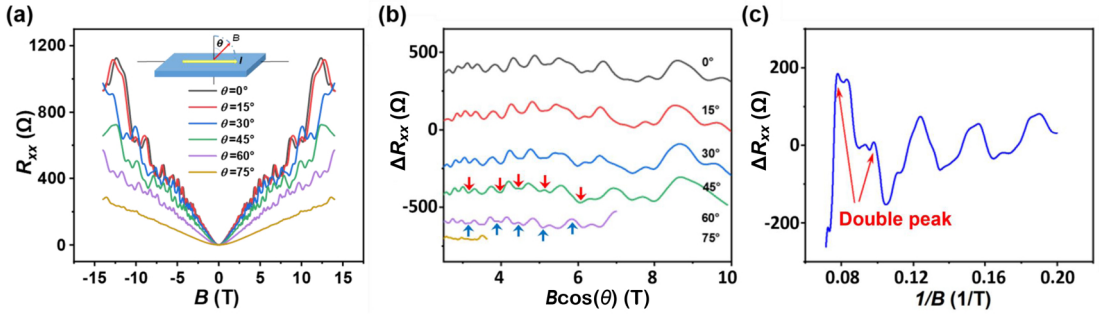

Fig. 4. (a) Original magnetoresistance curves under different tilted magnetic fields. (b) Angular-dependent SdH oscillations with the 180° phase shift when $\theta \geq 60°$. The presented data are obtained after subtracting the MR background. (c) Spin splitting of the SdH oscillation curve featured by the double peaks (red arrows) in the high magnetic-field region.

Here, we need to point out that the high-field spin splitting may also be correlated with the orbital effects induced by the tilted magnetic field,[43–45] and further studies (e.g., gate tuning and ultra-high-field measurements) are required to explicitly justify its physical origin. Accordingly, this high-field splitting feature can be attributed to the small effective mass, large effective g-factor and strong spin-orbit coupling in our AlGaSb/InAs QW heterostructures, thereafter allowing for efficient spin injection, manipulation and detection in spin-based applications.[46]

In conclusion, we have demonstrated the growth of high-quality $Al_{0.8}Ga_{0.2}Sb/InAs/Al_{0.8}Ga_{0.2}Sb$ QW thin films. Driven by the high mobility and large effective g-factor, the AlGaSb/InAs QW samples exhibit both a giant magnetoresistance and robust SdH oscillations up to 30 K; meanwhile, the strong spin–orbit coupling is manifested by the pronounced split SdH peaks at higher magnetic fields. Moreover, by tuning the Al-to-Ga ratio of the AlGaSb barrier, we have integrated strong spin–orbit coupling and high mobility in a single platform, paving the way for next-generation high-speed and energy-efficient spintronic devices. Besides, our work also shows that structural engineering provides an effective way to tailor the band alignment, which may enable the optimization of electrical parameters and/or topological orders for various applications.

Acknowledgements. This work was supported by the National Key R&D Program of China (Grant No. 2021YFA0715503), the Major Project of Shanghai Municipal Science and Technology (Grant No. 2018SHZDZX02), and the ShanghaiTech Material Device and Soft Matter Nano-fabrication Labs (No. SMN180827).

References

[1] Mikhailova M P, Moiseev K D, and Yakovlev Y P 2019 *Semiconductors* **53** 273
[2] Lelarge F, Dagens B, Renaudier J, Brenot R, Accard A, Van Dijk F, Make D, Le Gouezigou O, Provost J G, and Poingt F 2007 *IEEE J. Sel. Top. Quantum Electron.* **13** 111
[3] Luo J, Munekata H, Fang F, and Stiles P 1990 *Phys. Rev. B* **41** 7685
[4] Nichele F, Suominen H J, Kjaergaard M, Marcus C M, Sajadi E, Folk J A, Qu F, Beukman A J A, Vries F K D, Veen J V, Nadj-Perge S, Kouwenhoven L P, Nguyen B M, Kiselev A A, Yi W, Sokolich M, Manfra M J, Spanton E M, and Moler K A 2016 *New J. Phys.* **18** 083005
[5] Du R R 2022 *Memorial Volume for Shoucheng Zhang* (World Scientific) p. 243
[6] Xue F and MacDonald A H 2018 *Phys. Rev. Lett.* **120** 186802
[7] Wang R, Sedrakyan T A, Wang B, Du L, and Du R R 2023 *Nature* **619** 57
[8] Knox C, Li L, Rosamond M, Linfield E, and Marrows C 2018 *Phys. Rev. B* **98** 155323
[9] Iutzi R M and Fitzgerald E A 2015 *Appl. Phys. Lett.* **107** 133504
[10] Rybaltowski A, Xiao Y, Wu D, Lane B, Yi H, Feng H, Diaz J, and Razeghi M 1997 *Appl. Phys. Lett.* **71** 2430
[11] Lu Y, Zhou G, Li R, Liu Q, Zhang Q, Vasen T, Chae S D, Kosel T, Wistey M, and Xing H 2012 *IEEE Electron Device Lett.* **33** 655
[12] Kallaher R, Heremans J J, Van Roy W, and Borghs G 2013 *Phys. Rev. B* **88** 205407
[13] Rieger T, Grützmacher D, and Lepsa M I 2015 *J. Cryst. Growth* **425** 80
[14] Yoon S, Kam A, Gay B, Zheng H, and Ng G 1999 *Microelectron. J* **30** 745
[15] Adachi S 1987 *J. Appl. Phys.* **61** 4869
[16] Du P, Fang X, Zhao H, Fang D, Wang D, Gong Q, Kou X, Liu X, and Wang X 2020 *J. Alloy. Compd.* **847** 156390
[17] Du P, Fang X, Gong Q, Li J, Kou X, Zhao H, and Wang X 2019 *Phys. Status Solidi RRL* **13** 1900474
[18] Belser R B and Hicklin W H 1995 *J. Appl. Phys.* **30** 313
[19] Zahmani A H, Nishijima A, Morimoto Y, Wang H, Li J F, and Sandhu A 2010 *Jpn. J. Appl. Phys.* **49** 04DF14
[20] Ideshita S, Furukawa A, Mochizuki Y, and Mizuta M 1992 *Appl. Phys. Lett.* **60** 2549
[21] Li C Z, Li J G, Wang L X, Zhang L, Zhang J M, Yu D, and Liao Z M 2016 *ACS nano* **10** 6020
[22] Knap W, Skierbiszewski C, Dybko K, Lusakowski J, Siekacz M, Grzegory I, and Porowski S 2005 *J. Cryst. Growth* **281** 194
[23] Wolfe C M, Stillman G E, and Dimmock J O 1970 *J. Appl. Phys.* **41** 504
[24] Sugiyama Y 1994 *Sens. Actuators A Phys.* **40** 135
[25] Cheng H L 2010 *Spin-Orbit Coupling and Quantum Transport in Semiconductor Nanostructures* (Ph.D. dissertation, University of Michiga)
[26] Lorenzini P, Bougrioua Z, Tiberj A, Tauk R, Azize M, Sakowicz M, Karpierz K, and Knap W 2005 *Appl. Phys. Lett.* **87** 232107
[27] Bass J 1972 *Adv. Phys.* **21** 431
[28] Volcheck V and Stempitsky V 2019 *Journal of Physics: Conference Series* (unpublished)

[29] Zhang X B, Liu N Z, and Yao R H 2020 *Acta Phys. Sin.* **69** 157303 (in Chinese)
[30] Ohtomo A and Hwang H 2004 *Nature* **427** 423
[31] Tsukazaki A, Ohtomo A, Kita T, Ohno Y, Ohno H, and Kawasaki M 2007 *Science* **315** 1388
[32] Bimberg D 2008 *Semiconductor Nanostructures* (Springer Science & Business Media)
[33] Kunc J, Kowalik K, Teran F, Plochocka P, Piot B, Maude D, Potemski M, Kolkovsky V, Karczewski G, and Wojtowicz T 2010 *Phys. Rev. B* **82** 115438
[34] Karmakar C, Kaneriya R K, Malasi M, Rathod S, Kumar D, Chakravarty S, Upadhyay R B, Kumar P, Bhattacharya A N, and Joshi U S 2023 *Appl. Phys. Lett.* **122** 201601
[35] Onsager L 1952 *Philos. Mag. J. Sci.* **43** 1006
[36] Lifshitz I and Kosevich A 1956 *Sov. Phys. JETP* **2** 636
[37] Maurya V K, Patidar M M, Dhaka A, Rawat R, Ganesan V, and Dhaka R S 2020 *Phys. Rev. B* **102** 144412
[38] Doiron-Leyraud N, Szkopek T, Pereg-Barnea T, Proust C, and Gervais G 2015 *Phys. Rev. B* **91** 245136
[39] Nichele F, Kjaergaard M, Suominen H J, Skolasinski R, Wimmer M, Nguyen B M, Kiselev A A, Yi W, Sokolich M, and Manfra M J 2017 *Phys. Rev. Lett.* **118** 016801
[40] Nitta J, Lin Y, Akazaki T, and Koga T 2003 *Appl. Phys. Lett.* **83** 4565
[41] Fang F and Stiles P 1968 *Phys. Rev.* **174** 823
[42] Tarasenko S A 2002 *Phys. Solid State* **44** 1769
[43] Gustin C, Faniel S, Hackens B, Melinte S, Shayegan M, and Bayot V 2005 *Phys. Rev. B* **71** 155314
[44] Yang M J, Yang C H, Bennett B R, and Shanabrook B V 1997 *Phys. Rev. Lett.* **78** 4613
[45] Hu L H, Chen C C, Liu C X, Zhang F C, and Zhou Y 2017 *Phys. Rev. B* **96** 075130
[46] Ruskov R, Veldhorst M, Dzurak A S, and Tahan C 2018 *Phys. Rev. B* **98** 245424